Nanoscale

Accepted Manuscript

This article can be cited before page numbers have been issued, to do this please use: I. Choudhuri, S. Kumar, A. Mahata, K. S. Rawat and B. Pathak, *Nanoscale*, 2016, DOI: 10.1039/C6NR03282F.

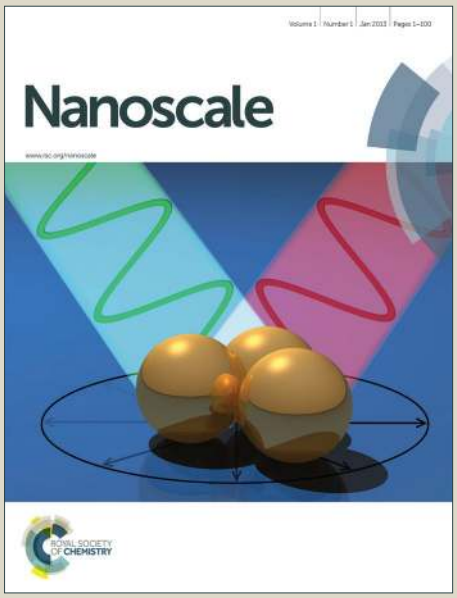

This is an *Accepted Manuscript*, which has been through the Royal Society of Chemistry peer review process and has been accepted for publication.

Accepted Manuscripts are published online shortly after acceptance, before technical editing, formatting and proof reading. Using this free service, authors can make their results available to the community, in citable form, before we publish the edited article. We will replace this *Accepted Manuscript* with the edited and formatted *Advance Article* as soon as it is available.

You can find more information about *Accepted Manuscripts* in the Information for Authors.

Please note that technical editing may introduce minor changes to the text and/or graphics, which may alter content. The journal's standard Terms & Conditions and the Ethical guidelines still apply. In no event shall the Royal Society of Chemistry be held responsible for any errors or omissions in this *Accepted Manuscript* or any consequences arising from the use of any information it contains.

ROYAL SOCIETY OF CHEMISTRY

www.rsc.org/nanoscale

Transition-Metal Embedded Carbon Nitride Monolayers: High-Temperature Ferromagnetism and Half-Metallicity

Indrani Choudhuri,[†] Sourabh Kumar,[†] Arup Mahata,[†] Kuber Singh Rawat,[†] Biswarup Pathak,[†,#,*]

[†]Discipline of Chemistry, School of Basic Sciences, Indian Institute of Technology (IIT) Indore, Indore, M.P. 452020, India

[#]Centre for Material Science and Engineering, Indian Institute of Technology (IIT) Indore, Indore, M. P. 452020, India

Email: biswarup@iiti.ac.in

1. Abstract

High-temperature ferromagnetic materials with planar surfaces are promising for spintronics applications. Using the state-of-the-art density functional theory (DFT) calculations, transition metal (TM = Cr, Mn, and Fe) incorporated graphitic carbon nitride (TM@gt-C_3N_4) systems are investigated for possible spintronics devices. Interestingly, ferromagnetism and half-metallicity observed in all the TM@gt-C_3N_4 systems. We find that Cr@gt-C_3N_4 is a nearly half-metallic ferromagnetic material with a Curie temperature of ~450 K. The calculated Curie temperature is noticeably high while compared to any planar 2D materials studied to date. Further, it has a steel-like mechanical stability and also possesses remarkable dynamic and thermal (500 K) stabilities. The calculated magnetic anisotropy energy (MAE) in Cr@gt-C_3N_4 is as high as 137.26 μeV/Cr. Thereby, such material with a high Curie temperature can be operated at high temperatures for spintronics devices.

Keywords: Half-metallicity, Ferromagnetism, gt-C_3N_4, Spintronics, High Curie Temperature

View Article Online
DOI: 10.1039/C6NR03282F

2. Introduction:

Atomically thin two-dimensional (2D) materials with planar surfaces have attracted considerable interest for their potential in spintronics devices.[1-2] Graphene and its analogues 2D materials with planar surfaces have shown tremendous potential due to their low dimensionality, electron confinement, and exceptional electronic/optical properties. Spintronics engages the study of the active manipulation of spin degree of freedom in materials. The spin properties should sustain above the room temperature for their practical applications. Layered 2D materials like graphene,[3,10-11] graphyne,[12] hexagonal boron nitride,[13] g-C_3N_4[14-17] and mono-layered MnO_2[18] have drawn great attention due to their unique and tunable optoelectronic and spin-electronic properties. However, most of the biocompatible 2D materials are nonmagnetic, which limits their application in Spintronics. Earlier reports suggest that transition metal (TM) incorporation on metal free 2D materials like graphene,[19-20] graphyne,[11] carbon nitride[16-17] induces some local magnetic moment and also leads to half-metallicity, where we can get 100% spin-polarized currents at the Fermi level. This is a very promising approach as this can significantly reduce the metal loading.

Recently, graphitic carbon nitride (g-C_3N_4) has received a lot of interest due to its wide applications in various fields.[14-23] However, carbon nitride exists in several allotropes, though the graphitic phase is the most stable phase under ambient conditions.[22-23] Previous reports show that the most stable planar graphitic (g-C_3N_4) sheet has two isomers: (i) heptazine-based g-C_3N_4 (gh-C_3N_4) and (ii) triazine-based g-C_3N_4 (gt-C_3N_4).[23] Interestingly, gh-C_3N_4 based materials have been widely investigated for spintronics and other applications.[16-17, 22-25.] However many times, the flat surface and thickness of 2D materials could not be controlled with precision. This suppresses the magnetic character of the 2D nanosheet. So, high-temperature ferromagnetic property in the atomically thin 2D nanosheet is one of the main challenges for the scientific community.

A large number of theoretical studies have been performed to investigate the ferromagnetic-antiferromagnetic coupling, half-metallicity and high magnetic anisotropy energy (MAE) for transition metal incorporated gh-C_3N_4 systems.[21] Zhang et al.[21] reported that transition metals strongly bind with gh-C_3N_4 than graphene and such transition metals embedded gh-C_3N_4 materials have been synthesized at elevated temperatures. [31-43] Recently, transition metal incorporated gh-C_3N_4[16-17,21] systems have been theoretically studied and revealed that such systems (TM@gh-C_3N_4) are metallic.[17-21] However, triazine-based g-C_3N_4 (gt-C_3N_4) structures have not been much studied.[26-28] Recently, B, Al and Cu atoms (nonmagnetic elements) embedded gt-C_3N_4 systems reported being half-metallic.[24] Furthermore, the ferromagnetism observed only in B and Al embedded gt-C_3N_4 systems. Interestingly, similar triazine-based g-C_4N_3 (C-doped gt-C_3N_4) motif shows intrinsic half-metallicity after carbon self-doping.[29-30] However, most of the intrinsic 2D materials are not magnetic, and their magnetic interactions are not strong enough to sustain the magnetism above room temperature. The creation of unsaturated p/d orbitals has received considerable attention for magnetism in 2D materials and remains an importance challenge for scientists.

Therefore, the gt-C_3N_4 based systems[24, 29] are unique and interesting as they show interesting magnetic properties (half-metallicity) compared to gh-C_3N_4 based systems. Hence, such interesting magnetic properties in gt-C_3N_4 based systems inspired us to study TM embedded gt-C_3N_4 systems. Thereby, we have investigated the first-row transition metal (Cr, Mn, and Fe) incorporated gt-C_3N_4 systems to create unsaturated p/d orbitals for possible spintronics materials by density functional theory (DFT) calculations.[24] The first-row transition metals are considered as they are abundant and show better magnetic properties.[25] The stability of the planar TM@gt-C_3N_4 sheets is very important for their synthesis and practical applications. Therefore, the stability of these sheets is confirmed systemically from the energetic (cohesive energy), mechanical (stress vs. strain), dynamical (phonon dispersion),

View Article Online
DOI: 10.1039/C6NR03282F

and thermal (molecular dynamics simulation) studies. The structural (geometry of the structures, oxidation state of metal), electronic (spin-polarized density of states and band structures) and magnetic (magnetic anisotropy energy, exchange energy, Curie temperature) properties are investigated to find out the principal requirements for memory and spintronics applications. Furthermore, Monte Carlo (MC) simulations are performed to predict the Curie temperature of TM@gt-C_3N_4 systems.

3. Computational Methods:

We have used spin-polarized density functional theory (DFT) calculations as implemented in the Vienna Ab initio Simulation Package (VASP).[44] The Perdew−Burke−Ernzerhof (PBE) exchange-correlation functional within the generalized gradient approximation (GGA)[45] is used for the present study. Projected augmented wave (PAW) method[46-47] is employed using an energy cut-off of 470 eV to describe the electronic wave functions. GGA+U method is used to properly describe the strongly correlated electrons in the partially filled d orbitals. [48] GGA+U method is used in our study, as it is well known that the GGA cannot properly describe strongly correlated systems containing partially filled d subshells.[49] Thus, we have divided electrons into two classes. The delocalized *s* and *p* electrons are described by the GGA method, whereas the localized *d* electrons are defined by the Coulomb and exchange corrections. This method not only improves excited-state properties such as energy gaps but also for ground-state properties (such as magnetic moments and interatomic exchange parameters). We have used correlation energy (U) of 4 eV and exchange energy (J) of 1 eV for TM d-orbitals. These U and J values have been well tested and used in many previous experimental studies on similar systems.[50-55] The vacuum is taken 12 Å along the z-axis to avoid any interaction between the two adjacent layers. The Monkhorst-pack[56] generated a set of 9×9×1 K-point is used to optimize all the structures. We have included the semi-empirical

View Article Online
DOI: 10.1039/C6NR03282F

DFT-D3 type of dispersion energy correction.[57] The convergence criteria for energy and force are set at 10^{-6} eV and 10^{-3} eV/Å, respectively. A set of 45×45×1 K-point is used for the spin-polarized density of state calculations (DOS). Bader charge analysis is performed[58-60] by using the Henkelman programme[61] with near-grid algorithm refine-edge method to understand the charge transfer process. Thermal stability of TM@gt-C_3N_4 systems is verified by carrying out Ab Initio Molecular Dynamics Simulations (AIMD) using canonical ensemble at 300, 500 and 1000 K with a time step of 1 fs for 5 ps. The nose thermostat model is used to control the temperature during the MD simulation.[62]

The energies of the ferromagnetic (FM) and antiferromagnetic (AFM) states of the (2×2) supercell geometry for each TM are calculated to understand the preferred magnetic coupling. The exchange energy (E_{ex}) per supercell is calculated using the following equation:

$$E_{ex} = E_{FM} - E_{AFM} \quad (1)$$

where E_{FM} and E_{AFM} denote the energies of ferromagnetic and antiferromagnetic states respectively. Similarly, the magnetic anisotropy energy (MAE) per supercell is calculated using the following equation:

$$MAE = E_{S0} - E_{S1} \quad (2)$$

where, E_{S0} is the energy of the system without employing any magnetic axis and E_{S1} is the energy in the presence of an easy axis. Here, the easy axis is the z-axis, which is perpendicular to the plane of TM@gt-C_3N_4 sheet [Supporting Information, text S2].

The spin density difference (SDD)[63] is plotted to understand the nature of the electron spin density on the unpaired electron in the pure/doped gt-C_3N_4 systems. The SDD is calculated using the following equation.

$$\rho_{SDD} = \rho^{Up} - \rho^{Down} \quad (3)$$

Here, ρ^{Up} and ρ^{Down} are the up and down electron spin density, respectively. In SDD, the positive and negative phases of the wave function for the different lobes are indicated by green and red colors, respectively. The direct mapping of the electron spin density is measured by the neutron diffraction in electron spin resonance (ESR) spectroscopy.[64]

4. Results & Discussion:

4.1 Pure gt-C_3N_4:

Previous reports[23] show that gt-C_3N_4 structure is ~0.2 eV less stable than the gt-C_3N_4 structure. However both the structues are synthesized experimentally.[27-28] Thus, a hexagonal unit cell (Figure 1a) of the gt-C_3N_4 structure is considered for our study[26-28]. There are two types of N (N_{in} and N_{link}; Figure 1a) present in gt-C_3N_4.[23] The calculated C-N bond lengths are 1.33 Å (C-N_{in}) and 1.46 Å (C-N_{link}).[23] The charge density of gt-C_3N_4 is plotted [Supporting Information, Figure S1(b), Table S1], which shows the electrons are highly delocalized over the planar surface.[22-23]

The spin-polarized density of states (DOS) shows [Figure S1, Supporting Information] that gt-C_3N_4 is a non-magnetic semiconductor with a wide band gap of 1.59 eV. This is very much in consistent with previous experimental and theoretical reports of 1.60-2.00 eV.[27-28] The partial projected DOS (pDOS) shows that the valence band (VB) and conduction band (CB) edges are mainly consisting of *2s* and *2p* orbitals of N_{in} and N_{link}, respectively [Supporting Information, Figure S2a-b].[22-23] Recently, nitrogen rich monolayers such as GaN [65] and MoN_2[66] have been reported for ferromagnetism. Here, magnetism occurs due to the presence of non-interacting N *2p* orbitals.

View Article Online
DOI: 10.1039/C6NR03282F

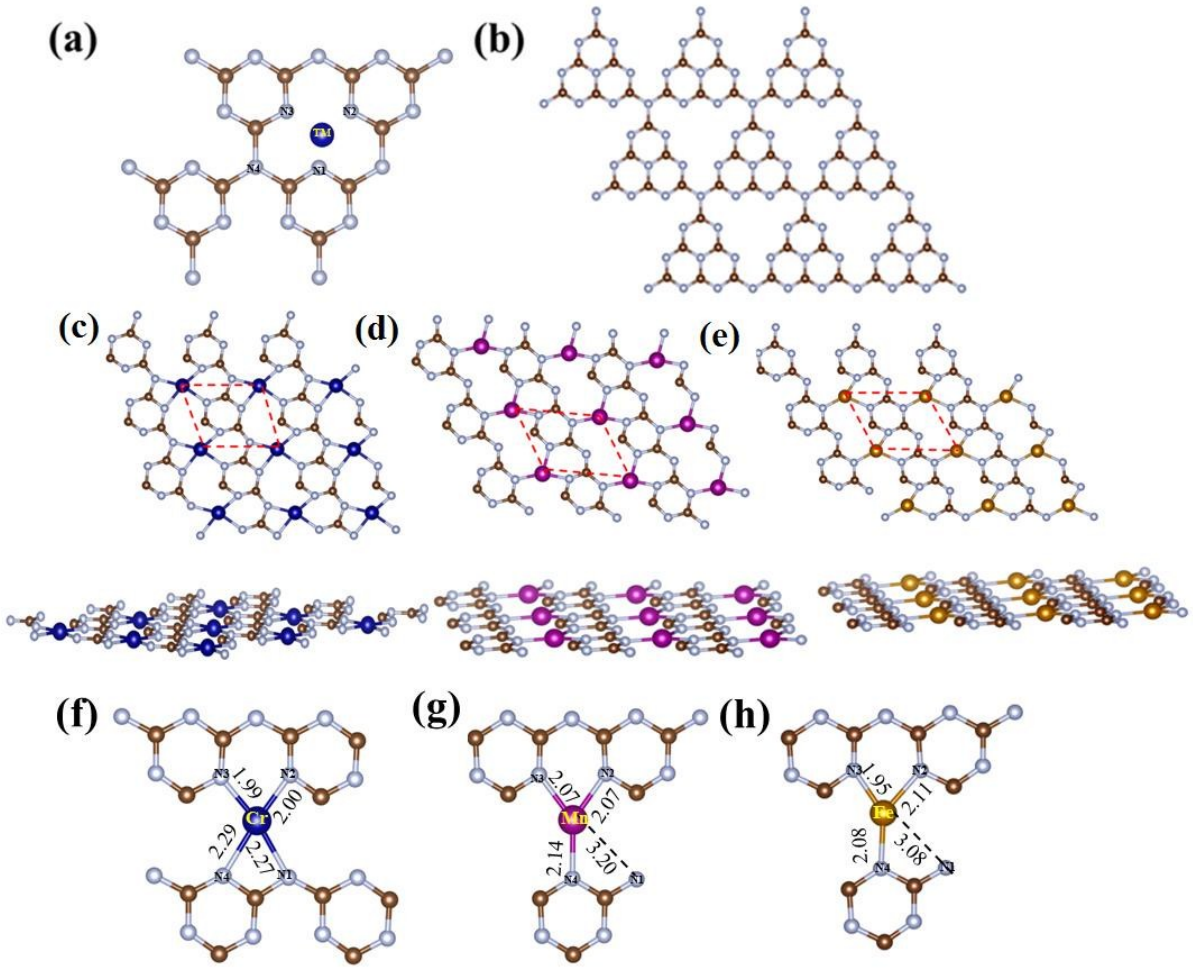

Figure 1: Schematic diagrams of (a) TM@gt-C_3N_4 and (b) gh-C_3N_4 systems. Optimized structures (top and side views) of (c) Cr@gt-C_3N_4, (d) Mn@gt-C_3N_4, and (e) Fe@gt-C_3N_4.. Here the unit cell is marked by a red dashed line. Important bond lengths (Å) in (f) Cr@gt-C_3N_4, (g) Mn@gt-C_3N_4, and (h) Fe@gt-C_3N_4 systems. Here, Grey, light blue, deep blue, pink and brown colours denote C, N, Cr, Mn, and Fe atoms, respectively.

4.2 TM@gt-C_3N_4:

Earlier transition metal incorporated gh-C_3N_4 systems have been synthesized[31-43] and recently Ghosh et al. theoretically predicted their magnetic properties.[17] For comparison, we have also studied the Cr, Mn and Fe incorporated gh-C_3N_4 structures and our results are compared with

View Article Online
DOI: 10.1039/C6NR03282F

the previous report on gh-C_3N_4. We find that our calculated cell parameters, binding energy, magnetic moments are very much in agreement [Table S2, Supporting Information] with the previous report on gh-C_3N_4. So, our level of theory is good enough for predicting new materials and their magnetic properties. TM embedded gt-C_3N_4 structures are optimized and shown in Figure 1.

Figure 1 shows that Cr forms a tetra-coordinated planar structure at the pore of gt-C_3N_4, where each Cr atom is bonded to four nitrogen atoms. Similarly, Mn and Fe embedded gt-C_3N_4 form a trigonal structure, where each metal atom is bonded to three nitrogen atoms. It suggests that the alternate hexagonal layers shift laterally to accommodate the TM atom. In Cr@gt-C_3N_4, the C-N bond distances (Supporting Information, Table S1) suggest that Cr-N1 and Cr-N4 are coordinating bonds, whereas Cr-N2 and Cr-N3 are covalent bonds. This indicates that Cr is in +II oxidation state in Cr@gt-C_3N_4. Similarly, we find that Mn and Fe atoms are in +II oxidation state in Mn@gt-C_3N_4 and Fe@gt-C_3N_4 systems, respectively.

The electrostatic potential (ESP) surface is plotted (using the VESTA[67]) on the total electron density surface to understand the nature of bonding between the TM and nitrogen atoms [Figure S11(a-f)]. The ESP plots show that the TM atoms are positively charged, whereas its surrounding N atoms are negatively charged. Bader charge analysis is also done to understand the charge distribution on each C, N and TM atoms by using Atoms in Molecules (AIM) theory. The important bond lengths and Bader charges of TM@gt-C_3N_4 systems are given in Table S1. It also shows that the TM atoms are positively charged and surrounded by negatively charged N atoms. In the TM@gt-C_3N_4, a significant amount of charge transfer occurs from gt-C_3N_4 sheet to TM atoms. We find that maximum charge transfer occurs in Fe@gt-C_3N_4 (0.68 $|e|$) system, whereas minimum in Mn@gt-C_3N_4 (0.46 $|e|$). This is because Fe (1.83) is more electronegative than Cr (1.66) and Mn (1.56). Our Bader charge analysis is also very much in consistent with our ESP findings [Supporting Information, Figure S11].

View Article Online
DOI: 10.1039/C6NR03282F

Thus, the gt-C_3N_4 motif changes due to the transition metal embedding, though the embedded structures remain planar. Considering the possibility of synthesizing a freestanding monolayer of TM@gt-C_3N_4, the sheet should have enough structural stability to be isolated. Thus, different types of stability are calculated and discussed in the following sections.

4.3 Energetic Stability:

The formation, binding, and cohesive energy calculations [Supporting Information text S1] are performed to investigate the energetic stability of the single layer TM@gt-C_3N_4 sheets. Our formation energy calculations predict that Cr@gt-C_3N_4 formation (0.21 eV) is favourable over Mn@gt-C_3N_4 (0.53 eV) and Fe@gt-C_3N_4 (0.59 eV) [Figure 1(a-c)] systems. However, Ghosh et al.[17] reported formation energies of -3.65, -4.48, -0.68, 1.40, 2.1, 1.40 eV for Cr, Mn, Fe, Co, Cu and Zn@gh-C_3N_4 structures respectively. Interestingly, systems (Co, Cu and Zn@gh-C_3N_4) with positive formation energy are realized experimentally.[31, 36-37] In fact, Fe@gh-C_3N_4 structure is also synthesized experimentally.[31] However systems (Cr, Mn@gh-C_3N_4) with negative formation energy are yet to be synthesized. Therefore, we believe that our predicted structures (Cr, Mn and Fe@gt-C_3N_4) can be experimentally realized. This could be due to the formation of tetra-coordinated Cr (Figure 1) in Cr@gt-C_3N_4, whereas tri-coordinated in Fe@gt-C_3N_4 and Mn@gt-C_3N_4. Furthermore, the calculated binding energies (E_B) of the metal atoms in the pore of gt-C_3N_4 are -7.39, -7.36, and -7.41 eV for Cr-, Mn- and Fe@gt-C_3N_4 systems, respectively. Thus, the TM atoms bind strongly in the pore of gt-C_3N_4. Additionally, we have calculated cohesive energies for metals to rule out the possibility of any cluster formation. Our calculated cohesive energies are -4.27, -3.12, and -4.46 eV for Cr-, Mn-, and Fe- bulk structures, respectively.[68] So, the possibility of cluster formation is low, as their binding energies are higher than their cohesive energies. Furthermore, the distance between the transition metal atoms is more than 5.0 Å, which reduces the possibility of metal-metal interaction.

View Article Online
DOI: 10.1039/C6NR03282F

4.4 Dynamic Stability:

The dynamic stability of TM@gt-C_3N_4 monolayer sheets is confirmed from the phonon frequency calculations. Phonon dispersion calculations are carried out in a supercell (2×2) geometry to reduce the constraint of periodic boundary condition. The lattice dynamics of TM@gt-C_3N_4 sheets are examined from their respective phonon dispersion plots (Figure S3). The Phonopy code[69] is used to calculate phonon properties through the density functional perturbation theory (DFPT).[70] Our phonon dispersion plot shows a very small imaginary frequency of 0.86 cm^{-1} (Figure S3) for Cr@gt-C_3N_4 when the phonon dispersion approaches to K or M. Such a small imaginary frequency value can be ignored and thus Cr@gt-C_3N_4 can be considered as a dynamically stable structure.[71-72] The absence of any large imaginary modes (>10 cm^{-1}) in any structures (Figure S3, Supporting Information) confirms that the TM@gt-C_3N_4 structures are dynamically stable. Besides, phonon dispersions are also calculated considering the dielectric effects and Figure S4 shows that Cr@gt-C_3N_4 has a small imaginary frequency of 1.03 cm^{-1}. Such a low imaginary frequency value (> 10 cm^{-1}) can be ignored[71-72] and Cr@gt-C_3N_4 can be considered as a dynamically stable structure.

4.5 Thermal Stability:

The thermal stability of TM@gt-C_3N_4 systems is assessed by performing ab initio molecular dynamics simulations (AIMD) using nose thermostat model as implemented in VASP. AIMD simulations are done to figure out the possibility of inter-conversion of the TM@gt-C_3N_4 sheet to any other conformers. Simulations are carried out on 2×2, and 3×3, supercell of the TM@gt-C_3N_4, using an NVT ensemble at 300K, 500K and 1000 K with a time step of 1fs (femtosecond) for 5 ps (picosecond). AIMD calculations are performed on supercell geometries to reduce the constraint of periodic boundary condition. At 300 K, Cr@gt-C_3N_4 remains planar throughout the simulation period (5 ps) though Mn@gt-C_3N_4 and Fe@gt-C_3N_4 become buckled [Figure S5-S10, Supporting Information]. Interestingly the Cr@gt-

View Article Online
DOI: 10.1039/C6NR03282F

C_3N_4 can withstand the temperature as high as 500 K. However, none of these structures retains the planar geometry at 1000 K. This is also reflected from the RMSD (Root mean square displacement) plots [Figure S8-S10]. The RMSD fluctuation is minimal up to 500 K but significant at 1000 K.

4.6 Mechanical Stability:

Strain technology is used to tune the geometrical and spin properties of the magnetic material. As supercell is fixed during MD simulations, it is necessary to assess the effect of lattice distortion on structural stability. Thus, the structural stability under the strain is very important for their synthesis and applications. We have investigated all the three TM@gt-C_3N_4 sheets for their mechanical stability and properties. The TM@gt-C_3N_4 monolayer sheets can be deformed either by tensile strain (by gradually increasing the lattice parameters) or compressive strain (by gradually reducing the lattice parameters) and following formula[73] is used to calculate the percentage (%) of strain applied:

$$\%\text{Strain} = \frac{a-a_1}{a} \times 100 \qquad (4)$$

where 'a' and 'a_1' are the lattice constants of the monolayer sheet before and after the strain. Tensile strains are applied along the in-plane uniaxial and biaxial directions to evaluate the mechanical stability of TM@gt-C_3N_4 monolayers. The effects of uniaxial and biaxial strains are investigated on the TM@gt-C_3N_4 supercell (2×2) structure. Atomic positions are relaxed at each strain until the forces on each atom are less than 10^{-2} eV/Å. Elastic limit is calculated from the stress-strain curve (Figure 2) under the tensile stretch.[74]

View Article Online
DOI: 10.1039/C6NR03282F

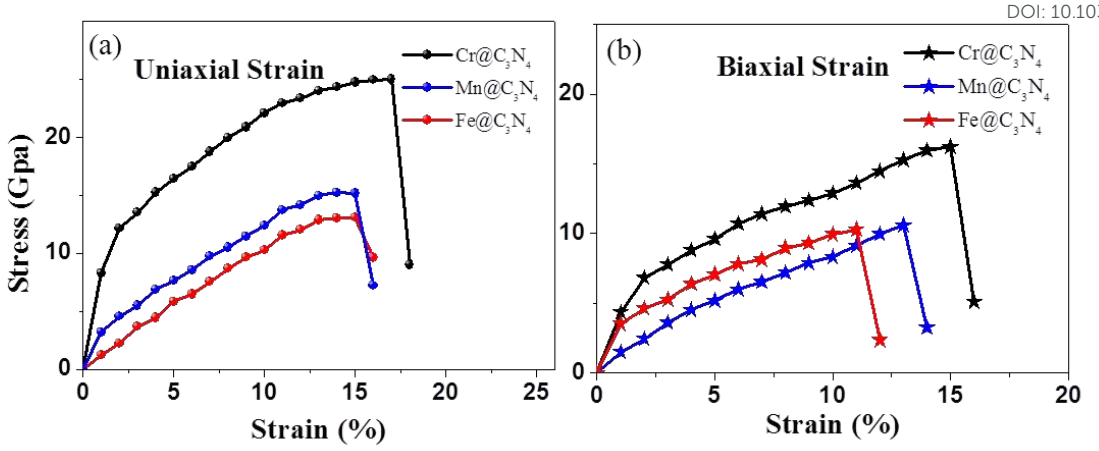

Figure 2: Strain [(a) Uniaxial and (b) equi-biaxial] vs. stress plots for TM@gt-C_3N_4 systems.

Figure 2 (a-b) shows that maximum stress occurs at 17%, 15% and 15% uniaxial strain for Cr@gt-C_3N_4, Mn@gt-C_3N_4, and Fe@gt-C_3N_4, respectively. So, the elastic limit of the planar Cr@gt-C_3N_4 is at 0.17 strain with a maximum stress of 24.95 GPa. However, the elastic limit decreases to 0.15 for Mn@gt-C_3N_4 and Fe@gt-C_3N_4 systems.

4.7 Mechanical properties:

Further, we have examined the mechanical properties of the TM@gt-C_3N_4 sheets. The mechanical properties of the sheet can be evaluated from the effect of lattice distortion on energetic stability. Here, we calculate the change in energy due to the strain to evaluate their mechanical properties. The elastic energy (U/per unit cell) near the equilibrium position can be calculated using the following formula:

$$U = 1/2C_{11}\varepsilon_{xx}^2 + 1/2C_{22}\varepsilon_{yy}^2 + C_{12}\varepsilon_{xx}\varepsilon_{yy} + 2C_{44}\varepsilon_{xy}^2 \qquad (5)$$

where C_{11}, C_{22}, C_{12} and C_{44} are the linear elastic constants where as ε_{xx}, ε_{xy}, ε_{yy} are the in-plane stress along the *x*, *y* and *xy* directions, respectively. The value of the elastic constants can be calculated by the polynomial fitting of strain *versus* energy plot.[75-77] The main criteria for mechanical stability are $C_{11} > C_{12}$ and $C_{44} > 0$. The value of C_{11} can be obtained under

View Article Online
DOI: 10.1039/C6NR03282F

uniaxial deformation, whereas C_{12} can be calculated by polynomial fitting under biaxial deformation. For all three TM@gt-C_3N_4 systems, we find that $C_{11} > C_{12}$ and $C_{44} > 0$. Thereby, the calculated elastic constants of TM@gt-C_3N_4 sheet satisfy all the criteria to be a mechanically stable sheet. Young's modulus (Y) and Poisson's ratio (PR) can be calculated from the elastic constants using the following equations.[77]

$$Y = (C^2_{11}-C^2_{12})/ C_{11} \quad (6)$$

$$PR = C_{12}/C_{11} \quad (7)$$

We find that Cr@gt-C_3N_4 has a higher Young's modulus (200.10 GPa) [Supporting Information, Figure S11 and Table S3] and Poisson's ratio (0.18) than Mn@gt-C_3N_4 and Fe@gt-C_3N_4 . Recently, Ruan et al. reported that elemental doping (C, B, S and P) in gh-C_3N_4 lowers the Young's modulus.[78] TM incorporation also shows a similar trend. Our calculated Young's modulus value for Cr@gt-C_3N_4 is 200.10 GPa, which is close to the Young's modulus value (180-200 GPa) of steel.[79-80] So, Cr@gt-C_3N_4 shows a steel like mechanical stability.

4.8 Electronic and Magnetic Properties:

Total electron density of states (TDOS) of the TM@gt-C_3N_4 systems derived to understand the electronic properties of these systems. The spin-polarized band structures and DOS are plotted (Figure 3-5) to understand the effect of TM in the pore of gt-C_3N_4.

View Article Online
DOI: 10.1039/C6NR03282F

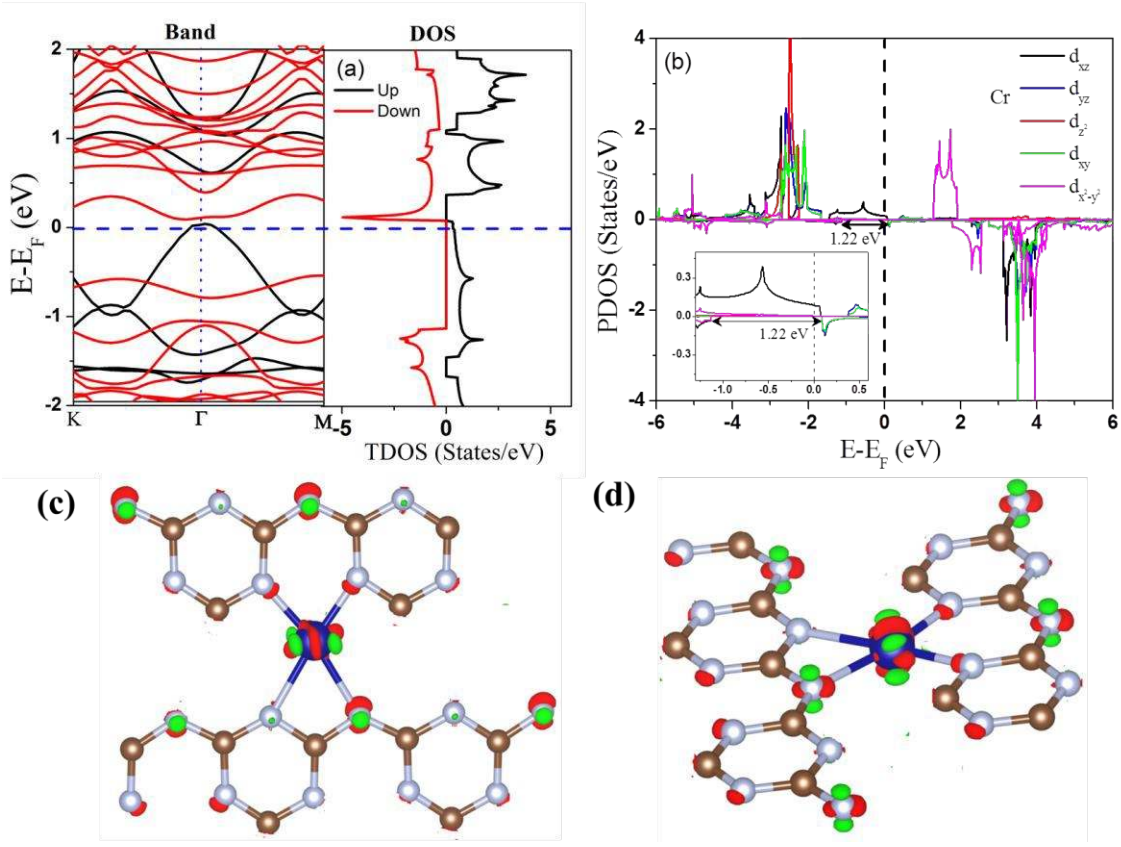

Figure 3: For Cr@gt-C_3N_4 system: (a) band structure and corresponding DOS plot; (b) d-orbital splitting, (c) top and (d) side views of spin density difference (SDD) plot. The positive and negative phases of the wave function are indicated by green and red colours. Here, isosurface value is set at 0.000012 e.Å^{-3}.

A careful investigation of spin-polarized band structures and DOS reveal interesting magnetic characters for TM embedded gt-C_3N_4 structures. In Cr@gt-C_3N_4, the crystal field stabilization energy (CFSE) is gained by Cr^{+2} ion due to the formation of a distorted square planar geometry [Supporting Information, Figure S13]. In a square planar geometry, the d-orbitals split into four bands. Generally, they split into a doubly degenerate d_π (out-of-plane d_{xz} and d_{yz} orbitals) and singly degenerate d_{z^2}, d_{xy}, and $d_{x^2-y^2}$ orbitals. Here we can find that d_{xz}, d_{yz}, d_{z^2}, and d_{xy} are singly occupied orbitals and they appear far from the Fermi level (Figure 3b).

View Article Online
DOI: 10.1039/C6NR03282F

However, the in-plane (d_{xy}, $d_{x^2-y^2}$) orbitals are little destabilized as they interact with the surrounding N 2p orbitals. In Cr(II), those low lying orbitals (d_{xz}, d_{yz}, d_{z^2} and d_{xy}) are singly occupied by four spin-up electrons. Thereby, the total magnetic moment in Cr@gt-C_3N_4 is 4 μ_B/Cr. This is very much in consistent with our spin density difference (SDD) plot (Figure 3c-d), where we find that the local magnetic moment highly localized on Cr.

Our detailed PDOS analyses (Figure S14) indicate that the spin-up channel mainly comprises of Cr 3d electrons, while spin-down channel mainly consists of N 2p electrons. Furthermore, the N 2p electrons in the spin-down channel are highly stabilized and thus creating a gap of 1.22 eV at the Fermi level. In contrary, the metallic nature of the spin-up channel shows that the main contribution at the Fermi level comes from the Cr 3d and C/N 2p orbitals. So our spin-polarized study indicates that Cr@gt-C_3N_4 is a half-metallic[81-82] system with 100% spin polarization at the Fermi. Gao et al. demonstated that Cr terminated (001) surface is nearly half-metallic as their one spin channel is metallic and other one is a nearly semiconductor.[81-82] However, in our case, the spin-up band crosses (at Γ-point) the Fermi level a little which corresponds to weak metallicity. So, such type of material can also be classified as a nearly half-metallic system. Here we predict that the spin-up electrons can be easily transported through the carbon-nitride framework with the help of hybridization of C/N 2p and Cr 3d orbitals.

Different competing magnetic states such as non-spin-polarized (NSP), ferromagnetic (FM) and antiferromagnetic (AFM)] states are studied to find out the magnetic ground states of TM@gt-C_3N_4 systems.[16-17] We find that the FM state is the ground state for the Cr@gt-C_3N_4 system. Further, the FM state is stable by 53.79 and 480.87 meV/TM [Supporting Information, Table S4] than the NSP and AFM states, respectively.

View Article Online
DOI: 10.1039/C6NR03282F

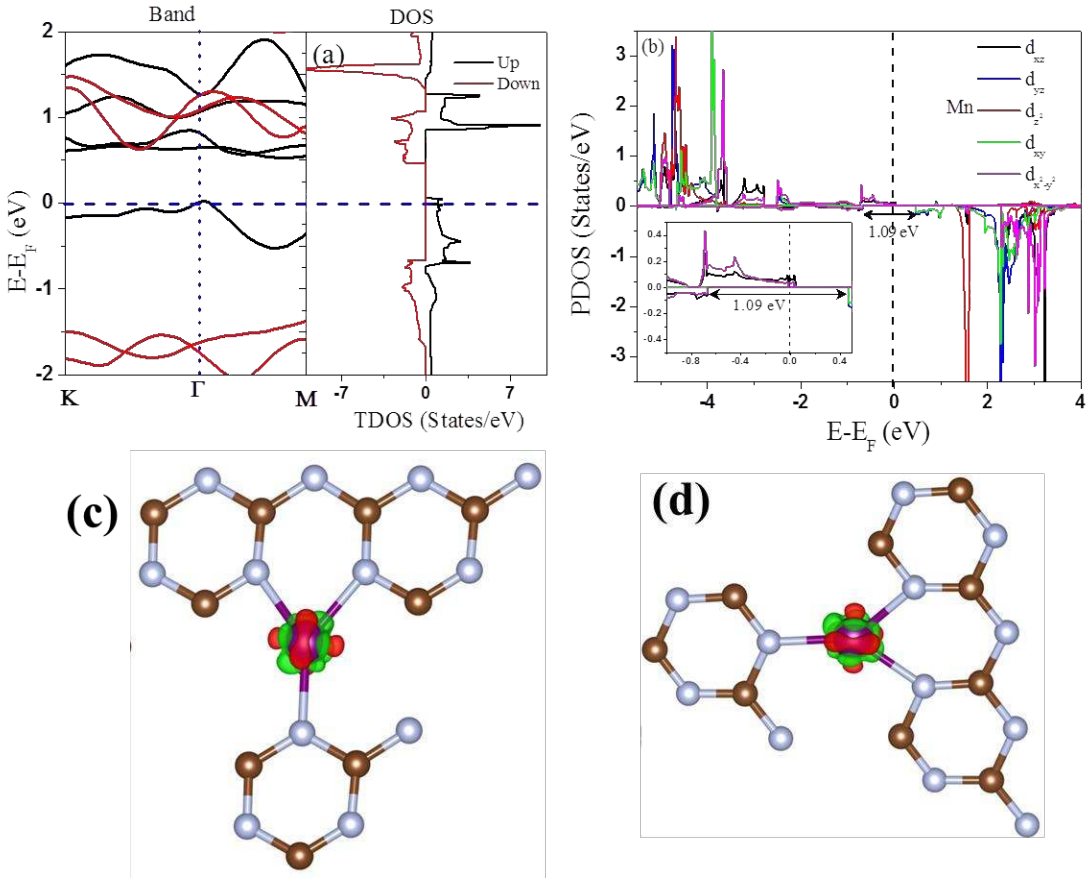

Figure 4: For Mn@gt-C_3N_4 system: (a) band structure and corresponding DOS plot; (b) d-orbital splitting; (c) top and (d) side views of spin density difference (SDD) plot. The positive and negative phases of the wave function are indicated by green and red colours. Here, isosurface value is set at 0.000012 e.Å^{-3}.

On the other hand, in Mn@gt-C_3N_4 (Figure 4a-b) system, the CFSE is gained due to the formation of a trigonal planar geometry. In the trigonal planar geometry, the d-orbitals split into four bands: two double degenerate bands (d_{yz}/d_{xz} and d_{xy}/$d_{x^2-y^2}$) and a single degenerate band (d_{z^2}). This is very much in consistent with our spin-polarized DOS (Figure 4b) of Mn@gt-C_3N_4. Here also, the out-of-plane orbitals (d_{yz}, d_{xz} and d_{z^2}) are stabilized with respect to the in-plane orbitals (d_{xy}, and $d_{x^2-y^2}$). The projected spin density (Figure 4b) shows that

the magnetic moment arises due to the singly occupied d_{yz}, d_{xz}, d_{z^2} d_{xy}, and $d_{x^2-y^2}$ orbitals of Mn, which appears at valence band region of -5.0 eV to -3.5 eV. Thereby, the Mn@gt-C_3N_4 system contains a local magnetic moment of 5 μ_B/Mn.

Our PDOS plot (Figure S14) indicates that the spin-up channel mainly comprises of Mn 3d and N 2p electrons, while spin-down channel mainly consists of N 2p electrons. Besides, the N 2p electrons in the spin-down channel are highly stabilized and thus creating a gap of 1.09 eV at the Fermi level. On the contrary, the metallic nature of the spin-up channel shows that the main contribution at the Fermi level comes from the Mn 3d and C/N 2p orbitals. So our spin-polarized study indicates that Mn@gt-C_3N_4 is a nearly half-metallic[81-82] system with 100% spin polarization at the Fermi, where the spin-up electrons can be easily transported through the carbon-nitride framework with the help of hybridization of C/N 2p and Mn 3d orbitals. Further, we find that the FM state is the ground state for the Mn@gt-C_3N_4 system and stable by 46.13 and 344.69 meV/unit cell with respect to NSP and AFM states, respectively.

View Article Online
DOI: 10.1039/C6NR03282F

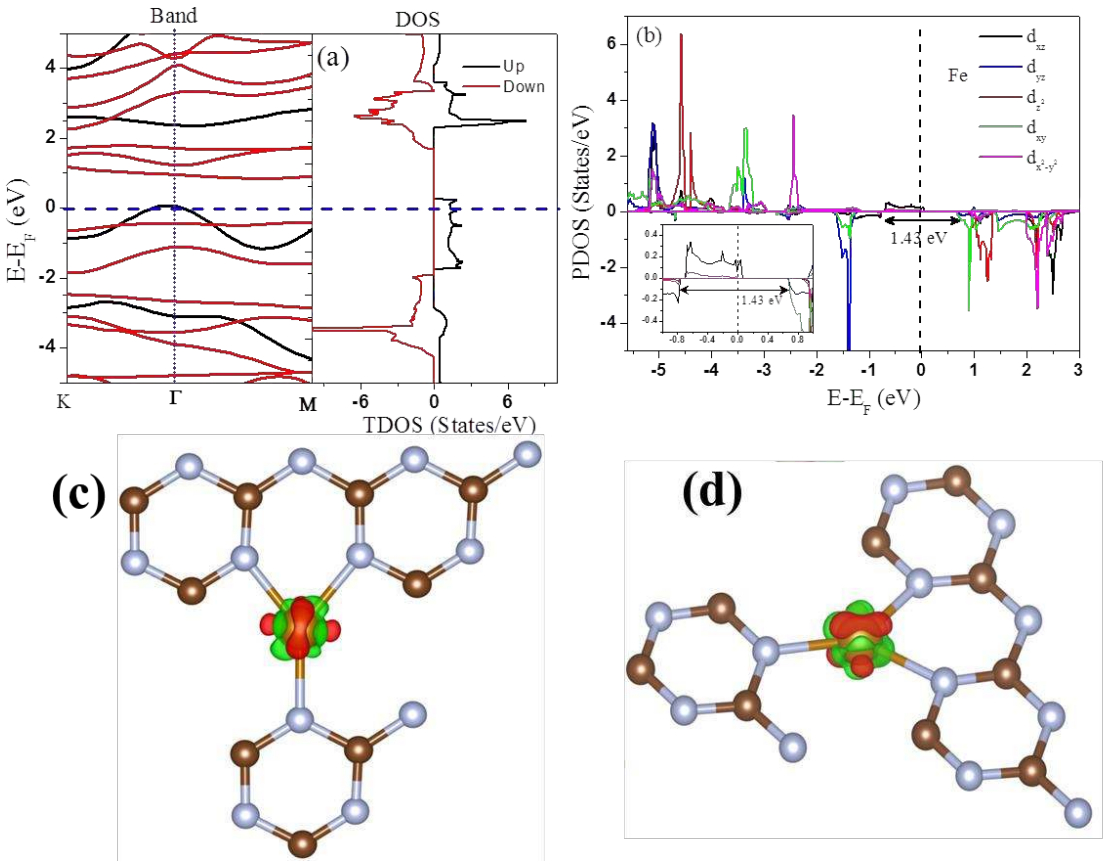

Figure 5: For Fe@gt-C_3N_4 system: (a) band structure and corresponding DOS plot; (b) d-orbital splitting, (c) top and (d) side views of spin density difference (SDD) plot. The positive and negative phases of the wave function are indicated by green and red colours. Here, isosurface value is set at 0.000012 e.Å^{-3}.

Similarly, Fe(II) forms a trigonal planar geometry in Fe@gt-C_3N_4. Our spin-polarized DOS (Figure 5b) shows that five singly occupied spin-up electrons are in d_{yz}, d_{xz}, d_{z^2}, d_{xy}, and $d_{x^2-y^2}$ orbitals. However, the d_{yz} orbital is occupied with a spin-down electron too. Thereby, the net effective magnetic moment in Fe@gt-C_3N_4 is 4 μ_B (Figure 5b) [Supporting Information, Figure S13]. Our SDD plot confirms that the magnetic moment mainly comes from Fe 3d orbitals. It can be clearly seen from Figure 5a that spin-up electrons would freely transport, while spin-down channel has a band gap of 1.43 eV. Thereby, the spin-down

View Article Online
DOI: 10.1039/C6NR03282F

channel shows a semiconducting nature, whereas spin-up channel remains metallic. Thus, Fe@gt-C_3N_4 is a nearly half-metallic[81-82] system with 100% spin polarization at the Fermi, where the spin-down electrons can be easily transported through the carbon-nitride framework with the help of hybridization of C/N 2p and Fe 3d orbitals. Further, we find that the FM state is the ground state in Fe@gt-C_3N_4, which is stable by 75.21 and 352.02 meV/unit cell over NSP and AFM states, respectively.

Therefore, the TM@ gt-C_3N_4 (TM = Cr, Mn, and Fe) systems are ferromagnetic and all these systems have exchange energy (E_{ex}) higher than 330 meV, which is necessary for a high curie temperature FM system.[12] One of the major conditions of a magnetic material for information technology applications is its magnetic anisotropy energy (MAE).[12] It helps the magnetic moment of a material to align with an easy axis, which is an energetically favourable axis for the spontaneous magnetization. We have calculated the MAE using the torque approach[21]. (Supporting Information, Text S2)

Previous studies show that 5d transition metal embedded gh-C_3N_4,[21] and 3d transition metal embedded graphyne generate large MAE.[12] So, here, we have calculated MAE for TM@gt-C_3N_4 systems. The non-collinear magnetic calculations with spin-orbit coupling are performed using the GGA+U level of theory. All magnetic moments are calculated with respect to a specified easy axis (z-axis). We find that Cr@gt-C_3N_4 shows MAE of 137.26 μeV, which is higher than the MAE of Mn@gt-C_3N_4 (119.83 μeV) and Fe@gt-C_3N_4 (116.39 μeV). So, TM@gt-C_3N_4 systems show high MAE as the FM and AFM states are separated by a large energy (>330 meV/unit cell). Thereby, such materials are promising for spintronics applications.

Classical spin Heisenberg Hamiltonian (H) is used to calculate the nearest neighbour exchange parameter (J_{ij}).

$$H = \sum_{<i,j>} J_{ij} S_i . S_j \quad (7)$$

View Article Online
DOI: 10.1039/C6NR03282F

Here, 'S' is the total magnetic moment per unit formula. We have already found that the FM is the ground state for all the three TM@gt-C_3N_4 systems. To develop a spintronics device, the Curie temperature (Tc) of the material should be comparable or higher than the room temperature. Here, the mean field theory (MFT)[49] [Text S3, Supporting Information] is adopted to estimate the Curie temperatures (T_C) of TM@gt-C_3N_4 systems. The calculated T_C values are in the range of 311-452 K for TM@gt-C_3N_4 systems [Supporting Information, Table S4]. Previously, Ghosh et al.[16-17] reported a high Curie temperature (~ 428 K) of Fe incorporated gh-C_3N_4. However, we find a high T_C of 452 K for Cr@gt-C_3N_4. Further, the calculated T_c values are 324 K and 311 K for Mn@gt-C_3N_4 and Fe@gt-C_3N_4 systems, respectively. Similarly, Monte Carlo (MC) simulations are performed [Text S3, Supporting Information] to estimate accurately the Curie temperature (T_C) of the Cr@gt-C_3N_4 system.[83-85] A supercell of 40 × 40 × 1 is constructed for Cr@gt-C_3N_4 system for the MC simulation, and the average magnetic moment per formula unit is taken after the system reached equilibrium at a given temperature. We have plotted (Figure 6) the magnetic moment (μ_B) vs. temperature (K) for Cr@gt-C_3N_4 system and we find that the magnetic moment per Cr atom starts gradually dropping at ~370 K and the paramagnetic states is achieved at ~440 K temperature, which indicates a magnetic phase transition. Thereby, the Cr@gt-C_3N_4 monolayer planar sheet can be a promising material for memory and spintronics devices.

View Article Online
DOI: 10.1039/C6NR03282F

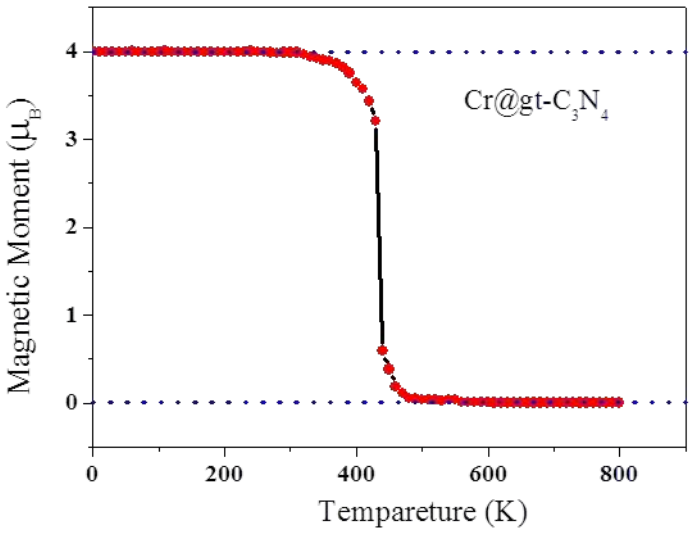

Figure 6. Variation of the total magnetic moment (μ_B) per formula unit of Cr@gt-C_3N_4 as a function of temperature (K).

5. Conclusions:

We have systematically studied the electronic and magnetic properties of the TM@gt-C_3N_4 (TM=Cr, Mn, and Fe) systems. A new class of 2D ferromagnetic nearly half-metallic materials are predicted with high Curie temperature and sizable magnetic anisotropy energy for their spintronics applications. The ferromagnetism in Cr@gt-C_3N_4 can survive up to 440-450 K based on our mean field and Monte Carlo calculations. Based on our calculations, we predict that Cr@gt-C_3N_4 system could be one of the high Curie temperature ferromagnetic half-metallic materials with 100% spin polarization at the Fermi in atomically thin 2D planar materials studied to date. Further, such materials are thermodynamically, dynamically, thermally, and mechanically stable and thereby can survive at high temperatures. Therefore, we predict that Cr@gt-C_3N_4 is a very promising material for high-temperature memory and spintronic devices.

6. Supporting Information:

The supporting information material is available free of charge on the RSC Publications website.

Computational details, optimized structures, phonon band structures, phonon DOS, MD simulations, RMSD plots at three different temperatures (300K, 500K and 1000K), spin-polarized TDOS, PDOS, Bader charges, mechanical properties (Young's' Modulus and Poisson Ratio), total electron densities and electrostatic potentials (ESP) plots, energy diagram of d-orbital splitting, magnetic properties calculation details and references.

7. Acknowledgments:

We thank IIT Indore for the lab and computing facilities. This work is supported by DST-SERB (EMR/2015/002057), New Delhi. I.C., S.K., K.S.R and A.M. thank MHRD, UGC MHRD for research fellowships.

8. Reference:

[1] J. Linder, J. W. A., *Nat. Phys*. 2015, **11**, 307.

[2] M. Misiorny, M. Hell, M. R. Wegewijs, *Nat. Phys*. 2013, **9**, 801.

[3] J. Hu, R. Wu, *Nano Lett*. 2014, **14**, 1853.

[4] L. Xiaohua, C. Adelmann, S. A. Crooker, E. S. Garlid, J. Zhang, M. K. S. Reddy, S. D. Flexner, C. J. Palmstrøm, P. A. Crowell, *Nat. Phys*. 2007, **3**, 197.

[5] S. Datta, B. Das, *Appl. Phys. Lett*. 1990, **56 (7)**, 665.

[6] S. Miwa, S. Ishibashi, H. Tomita, T. Nozaki, E. Tamura, K. Ando, N. Mizuochi, T. Saruya, H. Kubota, K. Yakushiji, T. Taniguchi, H. Imamura, A. Fukushima, S. Yuasa, Y. Suzuki, *Nat. Mater.* 2014, **13**, 50.

[7] C. Chappert, A. Fert, F. N. V. Dau, *Nat. Mater.* 2007, **6**, 813.

[8] S.V. Dijken, X. Jiang, S. S. P. Parkin. *Appl. Phys. Lett*. 2002, **80**, 3364.

[9] R. Qin, J. Lu, L. Lai, J. Zhou, H. Li, Q. Liu, G. Luo, L. Zhao, Z. Gao, W. N. Mei et al. *Phys. Rev. B* 2010, **81**, 233403.

[10] L. Li, R. Qin, H. Li, L. Yu, Q. Liu, G. Luo, Z. Gao, J. Lu, *Acs. Nano* 2011, **5**, 2601.

[11] J. Maassen, W. Ji, H. Guo, *Nano Lett*. 2011, **11,** 151.

[12] J. He, P. Zhou, N. Jiao, S. Y. Ma, K. W. Zhang, R. Z. Wang, L. Z. Sun. *Sci. Rep* 2013, **4**, 04014.

[13] A. Hashmi, J. Hong. *Sci. Rep* 2014, **4**, 04374.

[14] D. Gao, Q. Xu, J. Zhang, Z. Yang, M. Si, Z. Yan, D. Xue. *Nanoscale* 2014, **6**, 2577.

[15] K. Xu, X. Li, P. Chen, D. Zhou, C. Wu, Y. Guo, L. Zhang, J. Zhao, X. Wua, Y. Xie. *Chem. Sci*. 2015, **6**, 283.

[16] D. Ghosh, G. Periyasamy, S. K. Pati. *J. Phys. Chem. C* 2014, **118**, 15487.

[17] D. Ghosh, G. Periyasamy, B. Pandeyc, S. K. Pati. *J. Mater. Chem. C* 2014, **2**, 7943.

[18] M. Kan, J. Zhou, Q. Sun, v Kawazoe, P. Jena. *J. Phys. Chem. Lett*. 2013, **4**, 3382.

[19] H-X. Luan, C-W. Zhang, S-S. Li, R-W. Zhang, P-J. Wang. *RSC Adv*., 2013, **3**, 26261.

[20] C. B. Crook, C. Constantin, T. Ahmed, J-X Zhu, A. V. Balatsky, J. T. Haraldsen. *Sci. Rep.* 2014, **5** 12322.

[21] Y. Zhang, Z. Wang, J. Cao. *J. Mater. Chem. C* 2014, **2**, 8817.

[22] G. Dong, Y. Zhang, Q. Pan, J. Qiu, *J. Photochem. Photobiol. C: Photochem. Rev.* 2014, **20**, 33.

[23] X. Ma, Y. Lv, J. Xu, Y. Liu, R. Zhang, Y. Zhu, *J. Phys. Chem. C* 201**2**, **116**, 23485.

[24] B. Meng, W-z Xiao., L-l. Wang, L. Yue, S. Zhang, H-y. Zhang, *Phys. Chem. Chem. Phys.*, 2015, **17,** 22136.

[26] V. N. Khabashesku, J. L. Zimmerman, J. L. Margrave, *Chem. Mater*. 2000, **12,** 3264-3270.

[27] E. Kroke, *Angew. Chem. Int. Ed*. 2014, **53**, 11134.

[28] G. Algara-Siller, N. Severin, S. Y. Chong, T. Björkman, R. G. Palgrave, A. Laybourn, M. Antonietti, Y. Z. Khimyak, A. V. Krasheninnikov, J. P. Rabe, *Angew. Chem. Int. Ed.* 2014, **53**, 7450.

[29] A. Du, S. Sanvito, S. C. Smith, *Phyc. Rev. Lett*. 2012, **108**, 197207.

[30] J. S. Lee, X. Wang, H. Luo, S. Dai, *Adv. Mater*. 2010, **22**, 1004.

[31] X. Wang, X. Chen, A. Thomas, X. Fu, M. Antonietti, *Adv. Mater*. 2009, **21**, 1609.

[32] X. Wang, K. Maeda, A. Thomas, K. Takanabe, G. Xin, J. M. Carlsson, K. M. Domen, M. A. Antonietti. *Nat. Mater.* 2009, **8**, 76.

[33] X. Chen, J. Zhang, X. Fu, M. Antonietti, X. Wang. *J. Am. Chem. Soc*. 2009, **131**, 11658.

[34] X. Wang, K. Maeda, X. Chen, K. Takanabe, K. Domen, Y. Hou, X. Fu, M. Antonietti. *J. Am. Chem. Soc*. 2009, **131**, 1680.

[35] G. Zhang, Z-A. Lan, L. Lin, S. Lin, X. Wang. *Chem. Sci*., 2016, DOI: 10.1039/C5SC04572J.

[36] X. Zoua, R. Silva, A. Goswamia, T. Asefa, *Appl. Surf. Sci.* 2015, **357**, 221.

[37] Q. Liu, J. Zhang, *Langmuir* 2013, **29**, 3821.

[38] X. Song, H. Tao, L. Chen, Y. Sun, *Mater. Lett*. 2014, **116***,* 265.

[39] C. G. Liu, X. T. Wu, X. F. Li, X. G. Zhang, *RSC Adv.,* 2014, **4**, 62492.

[40] G. Zhang, S. Zang, X. Wang, *ACS Catal.* 2015, **5** (**2**)*,* 941.

[41] J. Xu, K-J. Long, Y. Wang, B. Xue, Y-X. Li, *Appl. Catal. A: General.* 2015, **496**, 1.

[42] L-F. Gao, T. Wen, J-Y. Xu, X-P. Zhai, M. Zhao, G-W. Hu, P. Chen, Q. Wang, H-L Zhang. *ACS Appl. Mater. Interfaces* 2016, **8**, 617.

[43] M. N. Nadagouda, R. B. N. Baig, R. S. Varma, S. Verma, *ACS Sustainable Chem. Eng.* 2016, **4**, 1661.

[44] G. Kresse, D. Joubert, *Phys. Rev. B* 1999, **59**, 1758.

[45] Perdew, J. P., Burke, K., Ernzerhof, M. *Phys. Rev. Lett*. **1996**, *77*, 3865.

[46] Perdew. J. P., Chevary. J. A., Vosko. S. H., Jackson, K. A., Pederson, M, R., Singh, D. J., Fiolhais, C. *Phys. Rev. B* **1992**, *46,* 6671.

[47] Anisimov, V. I., Aryasetiawan, F., Lichtenstein, A. I. J. *Phys.: Condens. Matter* **1997***, 9*, 767.

[48] Blochl, P. E. Projector Augmented-Wave Method. *Phys. Rev. B* **1994,** *50,* 17953-79.

[49] Zhou J., Sun, Q. *J. Am. Chem. Soc*. 2011, **133**, 15113.

[50] Okabayashi, J., Okabayashi, J., Rader, O., Mizokawa, T., Fujimori, A., Hayashi, T., Tanaka, M. *Phys. Rev. B* 1998, **58**, R4211.

[51] Sato, K., Bergqvist, L., Kudrnovsky, J., Dederichs, P. H., Eriksson, O., Turek, I., Sanyal, B., Bouzerar, G., Katayama-Yoshida, H., Dinh, V. A., Fukushima, T., Kizaki, H., Zeller, R. *Rev. Mod. Phys.* 2010, **82**, 1633.

[52] K. Sato, , P. H. Dederichs, H. Katayama-Yoshida, , J. Kudrnovsky, J. *Phys.: Condens. Matter* 2004, **16**, 5491.

[53] P. M. Panchmatia, B. Sanyal, *Chem. Phys*. 2008, **343**, 47.

[54] M. Bernien, J. Miguel, C. Weis, Md. E. Ali, J. Kurde, B. Krumme, P. M. Panchmatia, B. Sanyal, M. Piantek, P. Srivastava, K. Baberschke, P. M. Oppeneer, O. Eriksson, W. Kuch, H. Wende, *Phys. Rev. Lett.* 2009, **102**, 047202.

[55] A. B. Shick, J. Kudrnovsky, V. Drchal, *Phys. Rev. B* 2004, **69**, 125207.

[56] H. J. Monkhorst, J. D. Pack *Phys. Rev. B* 1976**, 13**, 5188.

[57] S. Grimme, J. Antony, S. Ehrlich, S. Krieg, *J. Chem. Phys*., 2010, **132***,* 154104.

[58] R. F. W. Bader. *Chem. Rev*. 1991, **91**, 893.

[59] G. Henkelman, A. Arnaldsson, H. Jónsson, *Comput. Mater. Sci*. 2006, **36**, 354.

[60] E. Sanville, S. D. Kenny, R. Smith, G. J. Henkelman, *Comput. Chem*. 2007, **28**, 899.

[61] W. Tang, E. Sanville, G. J. Henkelman, *J. Phys.: Condens. Matter,* **2009**, *21*, 084204.

[62] S. Nosé, , *J. Chem. Phys.* 1984, **81**, 511.

[63] A. Schweiger, G. Jeschke, Principles of Pulse Electron Paramagnetic Resonance, Oxford University Press: Oxford, England, 2001.

[64] IUPAC Gold Book.

[65] B. K. Rao, P. Jena, *Phys. Rev. Lett*. 2002, **89**, 185504.

[66] F. Wu, C. Huang, H. Wu, C. Lee, K. Deng, E. Kan, P. Jena, *Nano Lett*. 2015, **15**, 8277.

[67] K. Momma, F. Izumi, *J. Appl. Crystallogr*. 2011, **44**, 1272.

[68] Kittel, C., *Introduction to Solid State Physics*. Hoboken, NJ: John Wiley & Sons, 8th edition, **2005**.

[69] A. Togo, F. Oba, I. Tanaka, *Phys. Rev. B* 2008**, 78(13)**, 134106.

[70] S. Baroni, P. Giannozzi, A. Testa, *Phys. Rev. Lett*. 1987, **58**, 1861.

[71] Z. Zhang, X. Liu, B. I. Yakobson, W. Guo *J. Am. Chem. Soc*. 2012, **134**, 19326.

[72] J. Zhou, J. Huang, B. G. Sumpter, P. R. C. Kent, Y. Xie, H. Terrones, S. C. Smith, J. Phys. Chem. C 2014, 118, 16236.

[73] J. Zhang, X. Gong, B. Xu, Y. Xia, J. Yin, Z. Liu *Phys. Status Solidi B*, 2014, **251**, 1386.

[74] S. Zhang, J. Zhou, Q. Wang, C. Xiaoshuang, K. Yoshiyuki, P. Jena, *Proc. Natl. Acad. Sci. U.S.A*. 2015, **112**, 2372.

[75] R. C. Andrew, R. E. Mapasha, A. M. Ukpong, N. Chetty, *Phys. Rev. B* 2012, **85**, 125428.

View Article Online
DOI: 10.1039/C6NR03282F

[76] K. Wright, J. D. Gale, *Phys. Rev B* 2004, **70**, 035211.

[77] Y. Ding, Y. Wang *J. Phys. Chem. C* 2013, **117**, 18266.

[78] L-w. Ruan, Y-j Zhu., L-g. Qiu, Y-x. Lu *Vacuum*. 2014, **106**, 79.

[79] http://www.engineeringtoolbox.com/young-modulus-d_417.html

[80] The Stainless Steel Family" (PDF). Retrieved 8 December 2012.

[81] G. Y. Gao, K. L. Yao, *Appl. Phys. Lett*. 2014 **105**, 182405.

[82] G. Y. Gao, G. Ding, J. Li, K. Yao, M. Wu, M. Qian, *Nanoscale*, 2016, **8**, 8986.

[83] H. Jin, Y. Dai, B. Huang, M. Whangbo, *Appl. Phys. Lett.* 2009, **94**, 162505.

[84] R. F. L. Evans, W. J. Fan, P. Chureemart, T. A. Ostler, M. O. A. Ellis, R. W. Chantrell

J. Phys.: Condens. Matter, 2014*,* **26**, 103202.

[85] P. Asselin, R. F. L. Evans, J. Barker, R. W. Chantrell, R. Yanes, O. Chubykalo-Fesenko, D. Hinzke, U. Nowak, *Phys. Rev. B* 2010, **82**, 054415.

View Article Online
DOI: 10.1039/C6NR03282F

Table of Content (TOC):

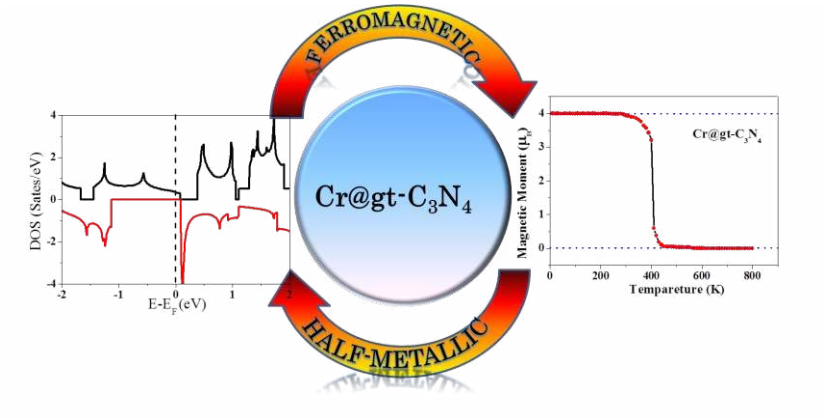

Transition-metal embedded carbon nitride (TM@gt-C_3N_4) monolayers for high-temperature ferromagnetism and half-metallicity